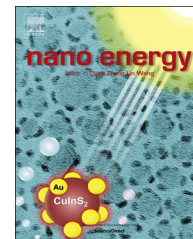Available online at www.sciencedirect.com

ScienceDirect

journal homepage: www.elsevier.com/locate/nanoenergy

RAPID COMMUNICATION

Scalable non-liquid-crystal spinning of locally aligned graphene fibers for high-performance wearable supercapacitors

Shaohua Chen[a], Wujun Ma[a], Yanhua Cheng[a], Zhe Weng[b], Bin Sun[a], Lu Wang[a], Wenping Chen[a], Feng Li[b], Meifang Zhu[a,*], Hui-Ming Cheng[b,*]

[a]State Key Laboratory for Modification of Chemical Fibers and Polymer Materials, College of Materials Science & Engineering, Donghua University, 2999 North Renmin Road, Shanghai 201620, China
[b]Shenyang National Laboratory for Materials Science, Institute of Metal Research, Chinese Academy of Sciences, 72 Wenhua Road, Shenyang 110016, China

Abstract
One-dimensional graphene fibers have attracted increasing interests due to their extraordinary mechanical strength, electrical conductivity and flexibility compared with two-dimensional graphene films/papers and three-dimensional foams/hydrogels/aerogels. Here, we developed a scalable non-liquid-crystal spinning process for the production of continuous graphene fibers with tailored structure for high-performance wearable supercapacitors. These fibers possessed surfaces with bark-like fine microstructure and different shaped cross-sections with locally aligned dense pores, depending on the jet stretch ratio (R) during spinning. Owing to this unique structure facilitating the access to, and diffusion of electrolyte ions, the specific capacitance reached 279 F g^{-1} (340 F cm^{-3}) at a current density of 0.2 A g^{-1} (0.244 A cm^{-3}) in 1 M H$_2$SO$_4$ when R=1.0. A flexible solid-state fiber supercapacitor assembled from these fibers showed a specific capacitance and energy density of 226 F cm^{-3} and 7.03 mWh cm^{-3} at 0.244 A cm^{-3}, respectively. We further demonstrated the proof-of-concept of wearable energy-storage by sewing three solid-state yarn supercapacitors in series into a textile, which was able

*Corresponding authors.
E-mail addresses: zhumf@dhu.edu.cn (M. Zhu), cheng@imr.ac.cn (H.-M. Cheng).

to power a light-emitting diode for more than 5 min after being charged. This non-liquid-crystal spinning strategy could be extended to the assembly of other two-dimensional nanomaterials into macroscopic fibers for applications in micro-devices, wearable electronics and smart textile.

Introduction

Graphene materials have attracted considerable attention from scientists and engineers, owing to their ultrahigh specific surface area, extraordinary mechanical, optical, electrical and thermal properties, together with their scalable low-cost production from natural graphite [1]. They have promising applications in energy storage devices [2-7], electronic components [8,9], functional nanocomposites [10-12], water treatment [13,14], hydrogen storage [15,16], etc. In most of these cases, graphene materials are used in the macroscopic forms of powders/particles [15,16], two-dimensional (2D) coatings/films/papers [2,3], or three-dimensional (3D) gels/foams [5,6,14], while one-dimensional (1D) macroscopic fibers of graphene were not reported until 2011 [17,18]. Graphene fibers are flexible, have high mechanical strength and electrical conductivity, and exhibit processing versatility [17,19,20]. Just like carbon fibers, they could be processed by twisting, weaving and knitting into light and flexible ropes, belts, fabrics and even 3D scaffolds. Similar to carbon nanotube (CNT) fibers [21], which have been widely explored in micro-/wearable energy devices [22-25], sensors [26,27] and actuators [28,29], graphene fibers would extend the capabilities of graphene in these fields, and could provide better performance [30,31] at a lower cost due to the significantly higher specific surface area of graphene.

Efforts have been devoted to prepare graphene fibers for miniature and wearable energy-storage applications, including the drawing assembly of graphene films [18], hydrothermal assembly of a graphene oxide (GO) dispersion in a pipeline or capillary column [20,32], and wet-spinning assembly of a liquid-crystal (LC) GO dispersion in water followed by reduction [17,19,33-35]. Among these, wet-spinning is the most scalable way to produce continuous long graphene fibers, yet it faces two challenges. The first one is to achieve a simple continuous spinning process compatible with industrial production. The continuous production of GO fibers is crucial for achieving uniform quality (e.g., the diameter and profile of their cross-section) and large-scale application. Because of the low concentration of a GO dispersion necessary for spinning [17,19,34], a large amount of water remains in wet GO fibers, leading to adhesion between the fibers after drying, which is a big issue for the production of bobbins of graphene fibers. The second challenge is the effective control of the structure of graphene fibers for high-performance energy-storage application. It is the surface morphology and inner structure that determine the mechanical, electrical and especially electrochemical performance of graphene fibers. For example, an all-graphene core-

sheath fiber, prepared by deposition of electrochemically reduced GO on the surface of a hydrothermally assembled GO fiber, shows a significantly higher capacitance than the pristine core fiber due to the large exposed surface area of the 3D-porous sheath [30]. Though conventional LC spinning can produce long graphene fibers, they often have a coarse surface with extended, slightly wrinkled, hydrophobic RGO sheets [17,33], and have a cross-section composed of compactly stacked, folded RGO sheets [19,33,34]. These structural characteristics are detrimental to the capacitive performance because of their poor affinity to aqueous electrolytes and the limited electrolyte ion diffusion inside those fibers [31]. In order to avoid this disadvantage, various fillers, such as CNTs and MoS_2, have been introduced to inhibit the restacking of RGO sheets and to create porous structures, resulting in hybrid fibers with enhanced specific capacitance but lower mechanical strength and higher costs [32,36,37]. To the best of our knowledge, simultaneous control of the surface morphology and internal structure of unfilled neat graphene fibers for high-performance wearable supercapacitors in a continuous spinning process has not been achieved to date.

Here we report a simple, scalable non-liquid-crystal (NLC) spinning method for the production of continuous RGO fibers with tunable structure for wearable supercapacitors. The resulting fibers possessed a macroscopic smooth surface with a willow-bark-like fine microstructure and a tunable pore structure with locally aligned RGO sheets over the radial plane, which could favor the access to, and fast diffusion of electrolyte ions. Owing to this unique structure, these undoped all-graphene fibers demonstrated excellent electrochemical performance compared with either neat or hybrid graphene fibers and CNT hybrid fibers prepared by conventional methods.

Experimental section

Preparation of RGO fibers

Graphite oxide was prepared by the oxidation of colloidal graphite with an average size of around 2 μm (Shanghai Yifan Graphite Co. Ltd) using the Hummers' method [38]. The weight ratio of graphite:$NaNO_3$:$KMnO_4$ was 1:1:5 and the oxidation time was 5 h. Graphite oxide (2 g) was added to deionized water (98 g) and sonicated for 1 h at an output power of 20 W using a digital ultrasonic processor (S-450D, Branson). The resulting 2 wt% dispersion was centrifuged at 5000 rpm for 10 min to remove unexfoliated particles. The supernatant with a pH value of 2 became more viscose after being left stationary for 6 h, and is denoted as the pristine

GO dispersion. A basified GO dispersion with a pH value of 11 was obtained by addition of 10 M NaOH solution (560 µL) into a supernatant (50 g) followed by sonication for 5 min, and it was free flowing in great contrast to the pristine one (Figure 1).

Continuous wet-spinning (see Movie S1 in the supplementary data) was carried out on the home-made apparatus illustrated in Figure 2a. For NLC spinning, the basified GO dispersion was injected into glacial acetic acid in a rotating Petri dish through a 27 G hollow needle (as spinneret, internal diameter = 210 µm) at a velocity of 1.5 m min^{-1}. The end of the needle was placed tangentially 30 mm away from the center of rotation, and the rotation speed was adjusted to 0.8, 1.6 and 2.4 rpm, corresponding to a jet stretch ratio R (the ratio of the stretching velocity to the injection velocity of the flow) of 0.5, 1.0, and 1.5, respectively. The wet fibers were drawn out vertically along the long infrared heater and wound onto a polytetrafluoroethylene pipe. For LC spinning, the pristine GO dispersion was spun at the same conditions, but only fibers with R values of 1.0 and 1.5 were successfully collected. These fibers were reduced by a HI solution (45 wt%) at 95 °C for 8 h, then washed with water and acetic acid alternatively 3 times, and finally dried at 80 °C under vacuum for 12 h to obtain RGO fibers.

Structural characterizations

Atomic force microscope (AFM) images of the GO sheets were taken in the tapping mode under ambient conditions on a Nanoscope IV system (Veeco Instruments, USA). Polarized optical microscope (POM) images of the GO dispersions and as-spun wet GO fibers were shot on an Alphaphot-2 optical microscope (Nikon, Japan). The rheological behavior of GO dispersions was evaluated by an ARES-RFS rheometer (TA Instruments, USA) using parallel plate geometry (50 mm diameter) with a gap of 8 ± 0.1 mm at 25 °C. The X-ray photoelectron spectroscopy (XPS) measurements were performed on an Axis Ultra DLD spectrometer (Kratos Analytical, UK) using a monochromatic Al Kα

source. The morphology of GO fibers and RGO fibers were observed on a SU8010 field-emission scanning electron microscope (SEM, Hitachi, Japan). The average cross-sectional area and perimeter of each sample were measured from SEM images of at least 5 single fibers by an image processing software. X-ray diffraction (XRD) patterns of RGO fiber bundles were recorded on a D/max 2550 PC diffractometer (Rigaku, Japan) with Cu Kα radiation ($\lambda = 1.5406$ Å) operating at 40 kV and 250 mA. The Herman orientation factor (H) was calculated using Eq. (1) [39,40]:

$$H = \frac{1}{2}(3\int_0^{2\pi} I \left| \sin\,\varphi \right| \cos^2\varphi d\varphi / \int_0^{2\pi} I \left| \sin\,\varphi \right| d\varphi - 1) \tag{1}$$

where I and ϕ are the intensity and azimuthal angle respectively.

The specific surface area (SSA) was evaluated using the methylene blue (MB) titration test [41]. In a typical test, 10 mg RGO fiber was added to 10 g water, then 100 µL 1 mg ml^{-1} of MB·3H$_2$O aqueous solution was added at regular intervals (3 h) while the mixture was shaken. The suspension was centrifuged and the concentration of MB in the supernatant was measured by a TU1901 UV–vis spectrometer (Purkinje General) at 665 nm. The mass ratio of adsorbed MB to RGO fibers was plotted against that of added MB to RGO fibers. SSA was calculated according to Eq. (2):

$$SSA = (m_{MB}/M_{MB}) \cdot A_c \cdot A_{MB}/m_{RGO} = 2.45 \\ \times 10^3 \cdot (m_{MB}/m_{RGO}) \tag{2}$$

where M_{MB} is the molar molecular weight (319.9 g mol^{-1}) of MB, A_c is Avogadro's number (6.02×10^{23}), A_{MB} is the area covered by one MB molecule (assumed to be 130 Å^2), and m_{MB}/m_{RGO} is the mass ratio of adsorbed MB to RGO fibers at the point where the decreasing slope is close to 0.98.

Performance characterizations

The linear density of RGO fibers was obtained by weighing a 10-meter-long filament on a XS microbalance (Mettler Toledo). Tensile tests were carried out at an extension rate of 2 mm min^{-1} with a gauge length of 10 mm on a XQ-1A
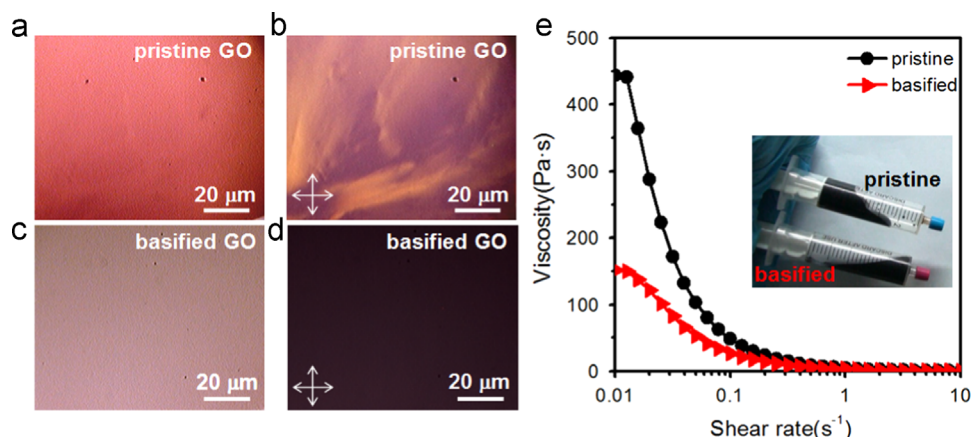

Figure 1 Microscopic and rheological characterizations of the GO dispersions. (a, c) Normal optical microscope (NOM) images and (b, d) corresponding POM images of (a, b) the pristine and (c, d) the basified 2 wt% GO dispersion. (e) Dependence of the viscosity of the pristine and basified 2 wt% GO dispersion on the shear rate. Inset is a photograph of GO dispersions in tilted syringes, indicating a better flowability of the basified dispersion.
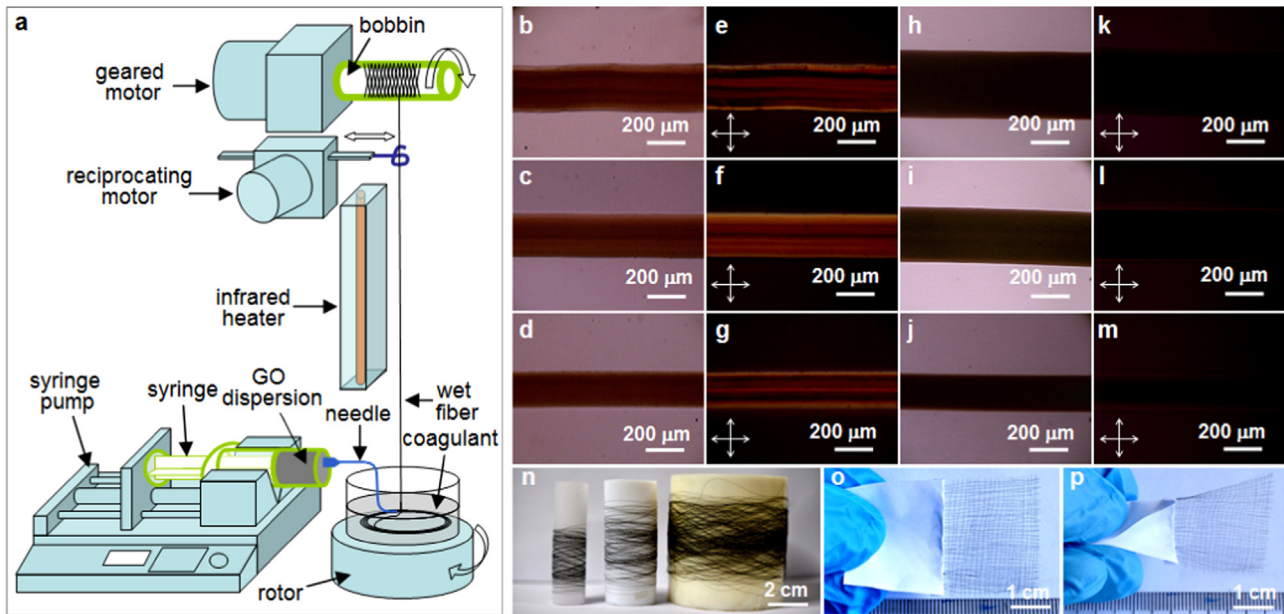
Figure 2 Wet spinning of GO fibers. (a) Schematic illustration of the wet-spinning process. The GO dispersion is injected into the rotating coagulant and solidifies into a wet fiber, which is dried by the infrared heater before being collected onto the bobbin. (b-d, h-j) NOM images and (e-g, k-m) corresponding POM images of the as-spun wet GO fibers obtained by (b-g) LC spinning and (h-m) NLC spinning at different jet stretch ratios: (b, e, h, k) $R=0.5$, (c, f, i, l) $R=1.0$ and (d, g, j, m) $R=1.5$. The NLC-spun wet fibers show very weak birefringence under POM. (n) Photograph of the NLC-spun GO fibers collected onto bobbins of different diameter. (o, p) A hand-woven fabric made from the RGO fibers: (o) unbent and (p) bent.

fiber tension tester (Shanghai New Fiber Instrument). The resistivity was measured by a two probe method on a PC68 high resistance meter (Shanghai Cany Precision Instrument). At least 5 filaments were tested for each sample and average values were reported.

Electrochemical tests of single RGO fibers were performed in a three-electrode cell on a CHI 660E electrochemical workstation (Shanghai Chenhua). A bundle of 5 RGO fibers (length=1.5 cm) was connected to stainless steel strip end to end by silver paste, and was used as a free-standing working electrode. A 0.5-mm-diameter Pt wire and Hg/Hg_2SO_4 electrode were used as the counter electrode and the reference electrode respectively. Cyclic voltammetry (CV) and galvanostatic charge-discharge (GCD) tests were conducted at scan rates from 2 to 100 mV s^{-1} and current densities from 0.2 to 2 A g^{-1}, respectively. Electrochemical impedance spectroscopy (EIS) was conducted at open circuit potential with an amplitude of 5 mV for frequencies from 10 mHz to 1 MHz. For a three electrode cell, the capacitance of the working electrode can be calculated from a full cycle of the CV curve by Eq. (3):

$$C = \frac{1}{2v\Delta U} \int |I|dU \qquad (3)$$

where C, v, U, ΔU and I are the capacitance, scan rate, potential, potential window and current, respectively. It can be also calculated from a galvanostatic discharge curve by Eq. (4):

$$C = It_d/(\Delta U - U_{drop}) \qquad (4)$$

where I, t_d, ΔU and U_{drop} are the constant discharge current, discharge time, potential window and potential drop, respectively.

To fabricate a solid-state flexible fiber supercapacitor, two RGO fibers (2 cm in length) were connected to stainless steel wires with silver paste, arranged in parallel, transferred onto a strip of 3 M magic tape, coated with a H_2SO_4/Polyvinyl alcohol (PVA)/H_2O (1/1/10 in weight) gel electrolyte, dried at room temperature and finally sealed by covering another strip of tape. Three yarn supercapacitors connected in series were similarly assembled from six bundles of five NLC-$R1.0$-RGO fibers (length=1.4 cm) and sewed into a textile. CV and GCD tests were carried out for these supercapacitors. For these two-electrode cells, the capacitance of a single electrode can be calculated from a full cycle of the CV curve by Eq. (5):

$$C = \frac{1}{v\Delta U} \int |I|dU \qquad (5)$$

It can be also calculated from a galvanostatic discharge curve by Eq. (6):

$$C = 2It_d/(\Delta U - U_{drop}) \qquad (6)$$

The mass-, length-, area- and volume-specific capacitance of a single electrode, respectively denoted as C_M (F g^{-1}), C_L (F cm^{-1}), C_A (F cm^{-2}) and C_V (F cm^{-3}), was calculated by dividing C by the mass, length, outer area and volume of one electrode, respectively. The energy density (E_M) and power density (P_M) of a solid-state supercapacitor were respectively calculated from discharge curves using Eqs. (7) and (8):

$$E_M = \frac{1}{8}C_M(\Delta U - U_{drop})^2 \qquad (7)$$

$$P_M = E_M/t_d \qquad (8)$$

where C_M, ΔU, U_{drop} and t_d are the mass-specific capacitance of a single electrode, potential window, potential drop and discharge time, respectively.

Results and discussions

The non-liquid-crystal spinning process

The average size of the GO sheets (shown in Figure S1) used for spinning was about 212 nm, and the thickness was around 1.1 nm, indicating dispersed GO as single-layer sheets in water. A pristine 2 wt% GO dispersion was found to have a pH value of 2, demonstrating the acidic nature of GO [42]. And it showed vivid colors under a polarized optical microscope (POM) (Figure 1b), indicating the formation of a LC phase [17]. Therefore, we refer to it as a LC GO dispersion and used it for LC spinning. Meanwhile, a basified 2 wt% GO dispersion with a pH value of 11 was obtained by the addition of a NaOH solution into a pristine one. By contrast, it showed no birefringence under POM (Figure 1d), implying that the LC phase has been disrupted. Thus it is referred to as a NLC GO dispersion and is used for NLC spinning. Interestingly, it was found that the pristine GO dispersion flowed slowly after sonication and even more slowly after resting, whereas the basified one flowed very easily all the time (inset in Figure 1e). This phenomenon is consistent with the remarkably lower viscosity of the basified dispersion than that of the pristine one at low shear rates (Figure 1e). Since the basified GO sheets are more negatively charged and repel each other [43], the hydrogen-bonding network in the pristine LC phase would be disrupted, resulting in good flowability of the NLC GO dispersion (Figure S2). It is this lower viscosity that would favor the smooth extrusion of the NLC GO dispersion and shear-induced alignment of GO sheets during spinning.

Continuous wet-spinning of GO fibers from both LC and NLC GO dispersions, respectively called LC spinning and NLC spinning, was performed on a home-made apparatus as illustrated in Figure 2a. The jet stretch ratio R was controlled by changing the rotation speed of the coagulant, on which the stretching velocity depends. Glacial acetic acid was shown to be an effective coagulant for both NLC and LC GO dispersion due to its acidic and highly hydrophilic nature. Acetic acid can absorb water from the extruded flow of a NLC or LC GO dispersion. Meanwhile, it can also diffuse into the flow and ionize with water and release protons, which inhibit the dissociation of acidic groups on GO sheets. As a result, GO sheets coagulate through strong hydrogen-bond interaction. It was found that both hydrophilic acetone and ethanol failed to coagulate the pristine GO dispersion, highlighting the importance of the acidity for the coagulant. A long infrared heater was used to dry the wet fiber before it was collected. This is essential to obtain a bobbin of a long single fiber without adhesion between adjacent loops. In a typical experiment, a GO fiber as long as 500 m was collected at 2.25 m min^{-1}, taking around 4 h, from a 12 ml GO dispersion without breaking. Fibers could be collected onto bobbins of different diameters as in industrial wet-spinning, which guarantees quality uniformity and facilitates post-processing and applications.

There is a large difference in the coagulation process between LC and NLC spinning. As shown in Figure 2b-g, LC-spun wet fibers were bright under a normal optical microscope and showed strong vivid color under POM, which indicates an ordered liquid-crystalline phase [19]. In contrast, NLC-spun wet fibers (Figure 2h-m) were very dark under NOM and showed very weak birefringence under POM, which is probably attributed to the disordered distribution of highly charged GO sheets that have undergone partial reduction by NaOH, as revealed by the XPS analysis (Figure S3). Interestingly, the diameters of NLC-spun wet fibers at $R = 0.5$ and 1.0 (346 and 293 μm, respectively) were larger than the inner diameter of the needle-spinneret (210 μm), and also larger than LC-spun ones at the same R. This obvious expansion in the radial direction is consistent with the observed shrinkage in the axial direction in the coagulation bath (Figure S4), and is possibly due to the repulsion between the aligned, negatively charged GO sheets in the flow after the release of the shear stress in the spinneret. On the contrary, the LC-spun wet fiber at $R = 0.5$ showed a minor expansion (diameter = 240 μm) with curly shapes (Figure S4), and was too fragile to be continuously collected. Because the extruded flow of the pristine GO dispersion (1.5 m min^{-1}) was naturally squeezed into curly shapes by the slower coagulant (0.75 m min^{-1}) due to very weak repulsion between liquid-crystalline GO nanosheets in the flow. Besides, the diameter of the wet fibers apparently decreased as R increased, indicating the importance of jet stretching on "locking" the flow-induced alignment of GO sheets. Therefore, a more porous structure is expected for NLC-spun RGO fibers at lower jet stretch ratios.

Structural characteristics of RGO fibers

Continuous RGO fibers were obtained by chemical reduction of the NLC- and LC-spun GO fibers in a HI solution, and are denoted as NLC-Rx-RGO and LC-Rx-RGO fibers, respectively, where x is the value of R. The morphology of the RGO fibers is shown in Figure 3. As for NLC-spun RGO fibers, their surfaces were rather smooth at the microscale but exhibited a fine structure at the nanoscale, similar to the bark of some trees, e.g., willow (Figure S5). This bark-like structure became less wrinkled and more aligned as R increased. At the same time, their cross-sectional profiles and pore structures changed remarkably with an increase of R: a "w"-shaped belt with large separate pores was observed when $R = 0.5$, a "t"-shaped 3-armed star with curved slit-like pores when $R = 1.0$, and an "x" shaped 4-armed star with narrow flat pores when $R = 1.5$. Note that as R was increased, the RGO sheets showed increased local alignment along the fiber arms in the radial plane and changed from wrinkled to wavy and finally to almost flat geometry. On the contrary, the LC-spun RGO fibers showed a coarse surface with a few large wrinkles and irregular multi-armed cross-section with disordered, compact stacks of RGO sheets. It is believed that the unique bark-like surface morphology and locally aligned pore structure of NLC-spun RGO fibers would favor the access to, and diffusion of, electrolyte ions.

The structure evolution from wet GO fibers to RGO fibers has been also investigated (Figures S6-S8), and a possible
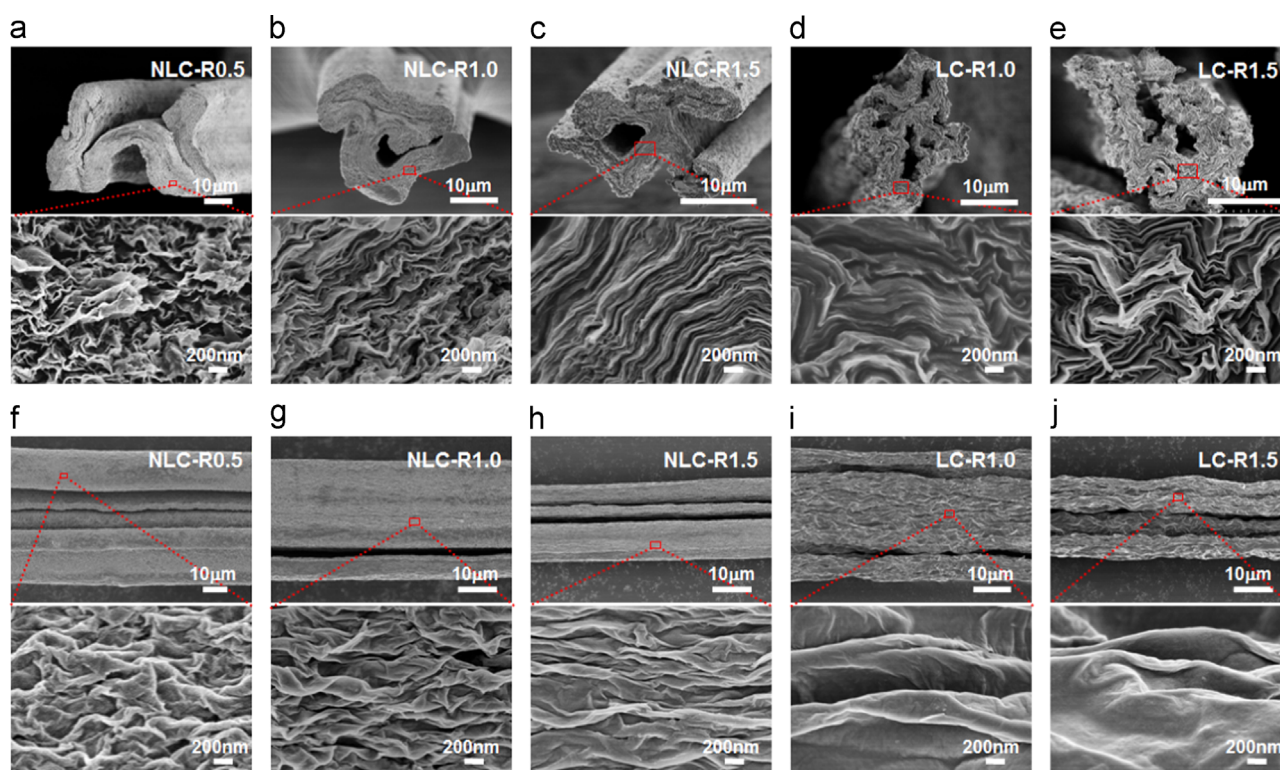
Figure 3 SEM images of (a-e) the cross-section and (f-j) the surface of RGO fibers prepared by NLC and LC spinning followed by reduction. (a, f) NLC-R0.5, (b, g) NLC-R1.0, (c, h) NLC-R1.5, (d, i) LC-R1.0, and (e, j) LC-R1.5.

fiber formation mechanism for NLC-spinning is proposed (Figure S9). Compared with original GO sheets, the basified GO sheets are more negatively charged, and therefore tend to have a greater mutual repulsion after extrusion. When the extruded flow is stretched, coagulated, and hot dried under tension, the GO sheets become aggregated with increasing local alignment as R increases (Figure S8) due to strong hydrogen-bonding interactions and the increasing stretching stress on the flow of low viscosity. After reduction by the HI solution, during which the physical form of a graphene oxide film can be maintained [44], the GO fibers are transferred to RGO fibers but undergo some deformation because of the volume shrinkage resulting from the loss of hydroxyl groups and the hot drying. Therefore, a separate pore structure with wrinkled RGO sheets is formed when $R=0.5$ due to the lack of stretching, and the pores become progressively more lamellar when R is increased to 1.5. Meanwhile, the negatively charged GO sheets at the flow surface are neutralized by acetic acid, and curl outward into nanofibrils (Figure S7) because of higher charges inside and stronger hydrogen-bonding interactions outside. After reduction, these nanofibrils are deformed to the bark-like surface of NLC-spun RGO fibers. As for the LC spinning, the GO liquid crystals in the viscous pristine dispersion are believed to suffer a twist at adjacent boundaries [17] and will be less locally aligned in the radial plane even after stretching due to the high viscosity of the LC GO dispersion. Therefore, when the extruded flow is drawn, coagulated and dried, multiple-folds form because of strong hydrogen bond interaction between GO sheets. Since the pristine GO sheets are less negatively charged, there is only a small difference between the outside and inside of the GO sheets when they meet the acetic acid, so fewer wrinkles form on the fiber surface.

The dependence of the structural characteristics of the RGO fibers on the spinning method and jet stretch ratio R were investigated, and the results are shown in Table 1. The condensed structure of RGO sheets in the fibers was characterized by XRD (Figure S10). Results showed that the interlayer spacing of RGO sheets in the NLC-spun RGO fibers decreased from 3.91 Å ($R=0.5$) to 3.74 Å ($R=1.0$), and finally to 3.72 Å ($R=1.5$), all of which are higher than that of natural graphite (3.35 Å) due to the imperfect stacking of defective RGO sheets. Azimuthal scan results indicated that the graphitic layers in the RGO fibers were preferentially oriented along the fiber axis, and the degree of orientation increased with the increment of R, in good agreement with SEM observations. This could be attributed to the larger shear stresses applied at higher R. It is found that the orientation parameter of the NLC-spun RGO fibers is a little lower than that of the LC-spun ones at the same R, but the difference is small when R is high. This is ascribed to the repulsion between the negatively charged GO sheets, which inhibits their stacking along the fiber axis during coagulation and thermal drying.

MB titration was used to evaluate the SSA of the RGO fibers (Figure S11). MB adsorption has been used to evaluate the SSA of clay materials [41] and carbon materials, including active carbon [45], thermally expanded graphite oxide and thermally-reduced porous graphene fibers [46,47]. There is a large difference between the values of SSA obtained by dry N_2 adsorption and wet MB adsorption.

Table 1 Structural characteristics and mechanical and electrical performance of RGO fibers.

Sample	Orientation parameter	SSA $[m^2\,g^{-1}]$	Linear density $[dtex]^a$	Strain to failure [%]	Specific stress $[cN\,dtex^{-1}]^b$	Specific modulus $[cN\,dtex^{-1}]$	Specific conductivity $[S\,cm^2\,g^{-1}]$	Strength [MPa]	Modulus [GPa]	Electrical conductivity $[10^2\,S\,m^{-1}]$
NLC-R0.5	0.648	419	13.9	6.6±0.7	0.933±0.063	29.0±0.9	7.34±0.07	104±7	3.23±0.10	8.15±0.08
NLC-R1.0	0.698	356	5.55	2.8±0.3	1.29±0.05	56.2±2.8	7.93±0.28	157±6	6.86±0.35	9.67±0.34
NLC-R1.5	0.723	231	3.35	2.3±0.2	1.17±0.03	61.4±2.5	8.59±0.47	208±6	10.9±0.4	15.3±0.8
LC-R1.0	0.725	273	4.91	2.7±0.1	0.950±0.025	46.6±1.7	28.7±2.4	138±4	6.77±0.25	41.7±3.5
LC-R1.5	0.732	168	3.16	1.5±0.1	1.02±0.03	50.8±1.9	30.0±0.9	150±5	7.50±0.28	44.2±1.3

^{a}1 dtex = 1 g km^{-1}.
^{b}1 cN dtex^{-1} = 10^5 N m kg^{-1}.

Since RGO fibers as supercapacitor electrodes work in an electrolyte solution, a wet MB adsorption test is preferred. As is shown in Table 1, the SSA of the NLC-spun RGO fibers obviously decreased with increasing *R*, which is consistent with the increase of the degree of compact stacking of the RGO sheets and the decrease of pore size observed from SEM images. Meanwhile, the NLC-spun RGO fibers have much higher SSA values than the LC-spun ones at the same *R* as a result of the poorer stacking of the RGO sheets. It is expected that a higher SSA would be beneficial for the electrochemical performance.

Mechanical and electrical performance of RGO fibers

The mechanical performance and electrical conductivity of the RGO fibers were calculated based on their linear density and average cross-sectional area (Figures S12-S16), and the results are summarized in Table 1 (Figure S17). It can be seen that the tensile strength and elastic modulus of the NLC-spun RGO fibers increased as the jet stretch ratio *R* was increased, with maximum values of 208 MPa and 10.9 GPa when *R* = 1.5. This is due to the smallest pore size and the highest orientation of the NLC-R1.5-RGO fiber. NLC-spun RGO fibers showed a little higher strength than LC-spun ones, which may be ascribed to their smoother surfaces, thicker arms and less large defects. Note that our porous NLC-R0.5-RGO fiber (101 MPa) is significantly stronger than the porous RGO fibers obtained by LC spinning using acetone as the coagulant (~48 MPa) [47]. And the strength of the NLC-R1.0/1.5-RGO fibers is comparable to that of those prepared by pipe-confined hydrothermal assembly or LC spinning using NaOH solution as coagulant (Table S1) [20,17,34]. It is believed that the strength could be further improved by using acetic acid coagulation containing divalent metal salts [19].

The electrical conductivities of the NLC-spun RGO fibers were calculated to be 815, 967 and 1530 S m^{-1} for *R* = 0.5, 1.0 and 1.5, respectively, which are comparable to that of drawing assembled porous graphene fibers and hydrothermally assembled RGO fibers (Table S1) [18,20]. It was found that the NLC-spun RGO fibers showed lower conductivity than the LC-spun ones at the same *R* (4170 and 4420 S m^{-1} for *R* = 1.0 and 1.5, respectively), which may be ascribed to their larger pore size, lower orientation along the fiber axis

and fewer edge-to-edge contacts between the RGO sheets. Nevertheless, it might be improved by thermal annealing treatment or by introducing conductive fillers such as carbon nanotubes [48,32].

Electrochemical behavior of RGO fibers and supercapacitors

Free-standing RGO fibers were used as working electrodes in order to demonstrate their potential as both the active material and the current collector (Figure S18). It was initially found that the original RGO fibers directly tested in 1 M H$_2$SO$_4$ exhibited moderate capacitive performance (Figure S19). Among these fibers, the NLC-R0.5-RGO fiber demonstrated the highest specific capacitances (51.4, 40.3 and 23 F g^{-1} at 2, 5 and 10 mV s^{-1}, respectively), due to its largest pore size and highest SSA. The macrospores in the NLC-R0.5-RGO fiber could be filled by 1 M H$_2$SO$_4$ at some degree under the electrical field during charging, while the tiny pores in the NLC-R1.0/1.5-RGO fibers could not be effectively filled by the electrolyte due to their higher capillary pressure. These capacitance values are still far superior to a CNT-coated carbon fiber (11 F g^{-1} at 10 mV s^{-1} in 1 M H$_2$SO$_4$) [49] and a twist-spun CNT fiber (14.7 F g^{-1} at 5 mV s^{-1} in 0.5 M H$_2$SO$_4$ [50]. The porous NLC-R0.5-RGO fibers were further assembled into a solid-state supercapacitor using H$_2$SO$_4$/PVA/H$_2$O gel electrolyte. This device showed a specific capacitance of 39.1 F g^{-1} at 0.2 A g^{-1} (0.15 mA cm^{-2}), which is significantly higher than that of a LC-spun compact RGO fiber supercapacitor (3.77 F cm^{-3} or less than 8.5 F g^{-1} at 0.1 mA cm^{-2}) [31], and comparable to that of a core-shell graphene fiber supercapacitor (~38 F g^{-1} at 0.2 A g^{-1}) [30], demonstrating the advantage of our NLC-spinning method. However, all of these values are still unsatisfactory compared with the theoretical double-layer capacitance of graphene. The main reason may be that RGO fibers could not be effectively wetted by 1 M H$_2$SO$_4$, as revealed by the observation that they floated on the surface of this electrolyte easily without obvious deformation (Movie S2), due to the hydrophobicity of RGO sheets and air-filled microspores. However, we noted that the capacitance of a NLC-R0.5-RGO fiber increased by an astonishing 137% after 4000 charge-discharge cycles at 0.8 A g^{-1} (Figure S19). This enhancement is possibly due to the electrochemically induced gradual wetting and expansion of the compact graphene layers by adsorption

and insertion of hydrated electrolyte ions, and implies high intrinsic capacitance of the NLC-spun RGO fibers.

Inspired by this observation, we developed a very simple way to enhance the capacitive performance of RGO fibers in H_2SO_4 electrolyte. A RGO fiber was firstly immersed in a 6 M KOH solution for 10 min before being tested in the 1 M H_2SO_4 solution. It was observed that once contacted with 6 M KOH, the RGO fiber immediately bent and then gradually recovered to close to its original shape (Movie S3), indicating an efficient diffusion of the KOH solution into the RGO fiber. This is because the acidic groups in the RGO fiber such as carboxyl groups, as indicated by XPS analysis (Figure S3), can react with basic OH⁻ ions and become repulsive COO⁻ ions, which render the expansion of compact RGO sheets and allow more KOH solution diffusing into the core. Since KOH reacts with H_2SO_4, the KOH-wetted RGO fiber can easily absorb H_2SO_4 solution and shows excellent affinity to 1 M H_2SO_4 electrolyte. The benefit of KOH-wetting was confirmed by the remarkably increased area of the CV curve of the KOH-solution wetted RGO fiber compared with either the original or ethanol-wetted RGO fiber (Figure S20). So we used this method to evaluate the capacitive behavior of all the RGO fibers in the 1 M H_2SO_4 solution. A 6 M KOH solution is not preferred as electrolyte for this evaluation, because it is not stable in air when used as gel electrolyte in a solid-state supercapacitor.

The electrochemical performance of the KOH-wetted RGO fibers in 1 M H_2SO_4 is shown in Figure 4 and Figure S21. Though less conductive than the LC-spun RGO fibers, the NLC-spun RGO fibers displayed two obvious redox peaks and much larger area in the CV curves at the same scan rate, due to their larger pore size, higher SSA and more locally aligned structure in the radial plane. The presence of redox peaks is attributed to the efficiently exposed residual oxygen-containing groups on RGO nanosheets, such as –COOH, –C=O and phenol groups, which can be reduced or oxidized in both acidic and basic electrolytes but not in neutral electrolytes (Figure S20a) [32,51]. This electrolyte effect has been also found for thermally reduced GO films as reported by Kim et al. [51]. Though wetted by KOH solution, the LC-spun RGO fiber showed much lower current density and very weak redox peaks in the CV curve, implying a tight stacking of RGO sheets. The results of GCD tests (Figure 4c) reveal that the KOH-wetted NLC-R1.0-RGO fiber exhibited the highest spe-

cific capacitance, because of its moderate pore size and local alignment. It can be imagined that the ion-diffusion path along the radial direction of a KOH-wetted NLC-R0.5-RGO fiber with the largest, disordered pores would be much longer than that of a KOH-wetted NLC-R1.0-RGO fiber with aligned pores (Figure S22). As for the KOH-wetted NLC-R1.5-RGO fiber with a highly aligned and dense structure, the ion diffusion would be hindered at some degree by the tight stacking of RGO sheets. These suppositions are confirmed by the electrochemical impedance spectra (Figure S21), where the NLC-R1.0-RGO fiber showed the smallest semicircle at the high frequency region. Since the KOH-wetted RGO fibers in 1 M H_2SO_4 are readily filled by the electrolyte, their capacitive behaviors are mainly diffusion-controlled, totally different from those of the pristine non-wetted ones which are mainly wetting-controlled (Figure S22).

Owing to the unique structure as well as the contribution of pseudo-capacitive oxygen-containing groups, the mass-specific capacitance of the KOH-wetted NLC-R1.0-RGO fiber was as high as 279 F g⁻¹ at 0.2 A g⁻¹, corresponding to an extraordinarily high volume-specific capacitance of 340 F cm⁻³ at 0.244 A cm⁻³ (0.085 mA cm⁻²) due to the dense pore structure. This value is superior to that of an electrolyte-mediated compact RGO film (255.5 F cm⁻³ at 0.1 A g⁻¹ in 1 M H_2SO_4) [52], and even much higher than that of a LC-spun RGO+CNT@CMC hybrid fiber (239 F cm⁻³ at 0.1 mA cm⁻² in 1 M H_2SO_4) [36], a hydrothermally assembled N-doped RGO/SWCNT hybrid fiber (305 F cm⁻³ at 0.0735 A cm⁻³ in 1 M H_2SO_4) [32], and a CNT/PEDOT hybrid fiber (167 F cm⁻³ at 10 mV s⁻¹ in 1 M H_2SO_4) [53]. The specific capacitance at 1.0 A g⁻¹ (1.22 A cm⁻³) reached 194 F g⁻¹ (237 F cm⁻³, Table S2) and is comparable to that of a 3D graphene hydrogel on a gold-coated polyimide film ($\sim$190 F g⁻¹ at 1 A g⁻¹ in 1 M H_2SO_4) [5]. And the value was still as high as 146 F g⁻¹ (178 F cm⁻³) at 2.0 A g⁻¹ (2.44 A cm⁻³), indicating a good rate performance considering no other current collector was used. Furthermore, it is worth noting that the mechanical strength of our NLC-R1.0-RGO fiber (157 MPa) is also much higher than that of N-doped RGO/SWCNT hybrid fiber (84 MPa) [32] and LC-spun RGO+CNT@CMC hybrid fiber (<116 MPa) [36], demonstrating the advantage of our spinning method.

A flexible solid-state fiber supercapacitor was assembled from KOH-wetted NLC-R1.0-RGO fibers (Figure 5a). CV and
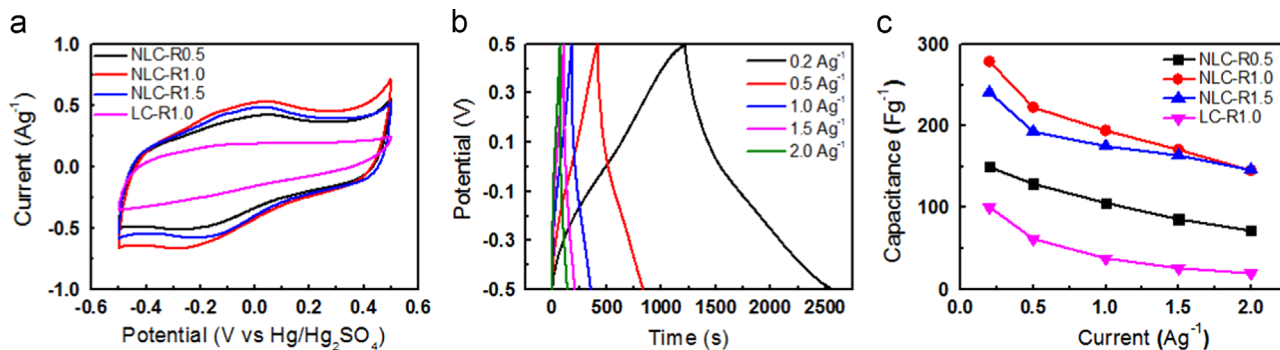

Figure 4 Electrochemical performance of RGO fibers in 1 M H_2SO_4. All the fibers were wetted by a 6 M KOH solution before tests. (a) CV curves at a scan rate of 2 mV s⁻¹. (b) GCD curves of NLC-R1.0-RGO fibers at different current densities. (c) Dependence of the specific capacitance on the current density.

GCD tests were performed in the potential range of 0–1.0 V, and the results are shown in Figure 5b and c, respectively. The *CV* curves were almost rectangular at low scan rates, and the GCD curves had a triangular shape, indicating a good charge transport between the two electrodes. The specific capacitance of the electrode was 185 F g^{-1} (226 F cm^{-3}, Table S3) at a current density of 0.2 A g^{-1} (0.244 A cm^{-3}, 0.085 mA cm^{-2}). Compared with other solid-state fiber supercapacitors (Table S4), this value is ∼60 times higher than that of a LC-spun compact RGO fiber (CaCl$_2$ solution as coagulant) (3.77 F cm^{-3} at 0.1 mA cm^{-2}) [31], much higher than that of a LC-spun MoS$_2$/RGO hybrid fiber

(30 F cm^{-3} at 0.1 μA) and a core-shell all-graphene fiber (∼38 F g^{-1} at 0.2 A g^{-1}) [37], superior to that of a LC-spun RGO+CNT@CMC hybrid fiber (158 F cm^{-3} at 0.1 mA cm^{-2}) [36] and a hydrothermally assembled N-doped RGO/SWCNT hybrid fiber (∼200 F cm^{-3} at ∼0.27 A cm^{-3}, excluding the gel electrolyte) [32]. As shown in Figure 5d, the capacitance decreased to 65.2 F g^{-1} (79.5 F cm^{-3}) when the current density increased to 2.0 A g^{-1}, which can be ascribed to the dense pore structure. And a capacitance retention rate of 92% was observed after 1000 charge-discharge cycles (Figure 5e) at 1.0 A g^{-1}. The small capacitance loss may be attributed to the gradual degradation of redox groups
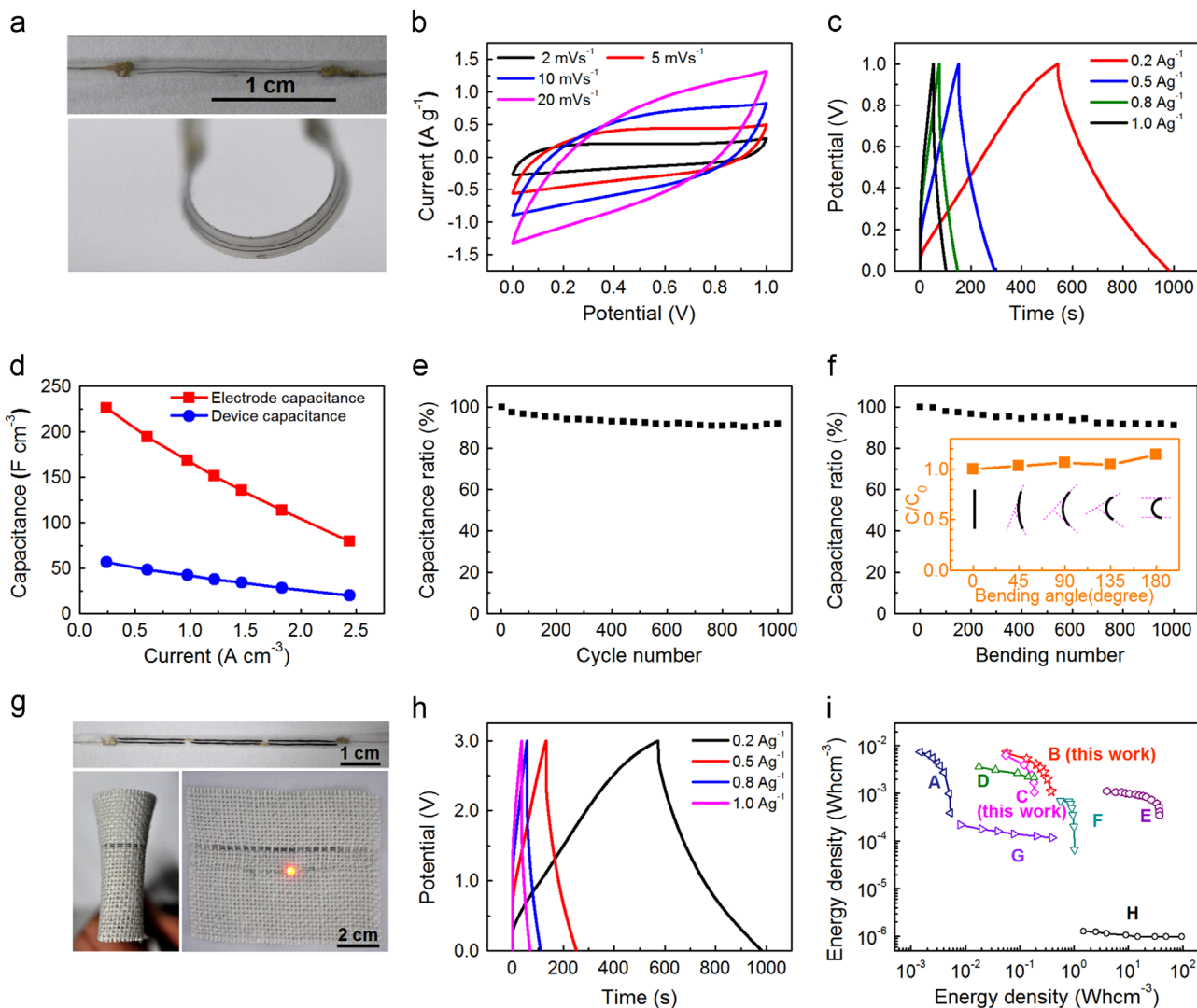

Figure 5 Electrochemical performance of solid-state supercapacitors assembled from NLC-*R*1.0-RGO fibers. (a) Photo of a 1 V fiber supercapacitor assembled from two single RGO fibers as electrodes at straight and bent state. (b-f) Performance of the supercapacitor as shown in (a). (b) *CV* curves. (c) GCD curves. (d) Dependence of the volume-specific capacitance on the current density. (e) The GCD cycling performance at a current density of 1 A g^{-1}. (f) Capacitance stability during bending from 0° to 180° for 1000 times. The inset is the variation of the capacitance at different bending angles. (g) Photo of a 3 V yarn supercapacitor assembled from six bundles of RGO fibers. This device was sewed into a textile and could power a red light-emission diode (LED) for ∼5 min after being charged to 3 V at a scan rate of 10 mV s^{-1} (5 min). (h) GCD curves of the device as shown in (g). (i) Ragone plots of (A) a commercial 4 V/500 μAh thin Li-film battery [54]; (B) the 1 V fiber supercapacitor as shown in (a); (C) the 3 V yarn supercapacitor in-series as shown in (g); (D) a CNT/RGO@CMC hybrid fiber supercapacitor [36]; (E) a PEDOT/CNT fiber supercapacitor [53]; (F) a commercial 2.75 V/44 mF active carbon supercapacitor [55]; (G) a MnO$_2$-loaded carbon fiber super-capacitor [56]; and (H) a commercial 3 V/300 μF Al-electrolytic capacitor [55].

[51] and the evaporation of water in the gel electrolyte to the air. Figure 5f shows that the capacitance increased slightly by 14% when the device is bent to 180°, and retained 91% after cyclic bending from 0° to 180° for 1000 times, demonstrating excellent flexibility and bending stability of this device.

In order to demonstrate the concept of wearable supercapacitors, three solid-state yarn supercapacitors connected in series were similarly assembled and further sewed into a textile (Figure 5g). This integrated device was flexible and was able to power a red LED for ~5 min after being charged to 3 V at a scan rate of 10 mV s^{-1} (Figure S23). The GCD curves in Figure 5h indicate that this device could be reversibly charged and discharged to 3 V and exhibited a device capacitance of 1.12 mF at a current of 7.45 μA, corresponding to an electrode capacitance of 179 F g^{-1} (218 F cm^{-3}) at a current density of 0.2 A g^{-1}. Figure 5i compares the energy and power densities of this 3 V yarn supercapacitor and the aforementioned 1 V fiber supercapacitor with some other fiber supercapacitors as well as some commercial energy-storage devices. The 1 V fiber supercapacitor possessed an energy density of 5.76 Wh kg^{-1} (7.03 mWh cm^{-3}) at an power density of 47.3 W kg^{-1} (57.7 mW cm^{-3}). This value is two orders of magnitude higher than that of an asymmetric supercapacitor assembled from carbon-fiber fabrics grown with MnO_2 nanowires and Fe_2O_3 nanotubes (0.55 mWh cm^{-3}) [57], much more superior to that of a CNT/PEDOT hybrid fiber supercapacitor(1.4 mW cm^{-3}) [53] and a RGO+CNT@CMC hybrid fiber supercapacitor (3.5 mWh cm^{-3}) [36], and also comparable with that of a N-doped RGO/SWCNT hybrid fiber supercapacitor (~6.3 or ~10.5 mWh cm^{-3} including or excluding the gel electrolyte, respectively) [32] and an asymmetric supercapacitor assembled from N-doped and MnO_2-loaded RGO/SWCNT fibers (~5 mWh cm^{-3} including the gel electrolyte) [58]. Compared with the 1 V fiber supercapacitor, the 3 V yarn supercapacitor had a bit lower power densities but similar energy densities (1.07-6.28 mWh cm^{-3}), which are three orders of magnitude higher than those of a commercial 3 V/300 μF Al-electrolytic capacitor [55], about 10 times higher than those of a commercial 2.75 V/44 mF active carbon supercapacitor [55], and even comparable to those of a commercial 4 V/500 μAh thin Li-film battery [54]. Meanwhile, the power densities (55.6-185 mW cm^{-3}) are ~40 times of those of the thin Li-film battery, though lower than those of the active carbon supercapacitor and the Al-electrolytic capacitor. Therefore, further improvement in the power density of our supercapacitors will be focused in the future.

Conclusions

In summary, we developed a simple and scalable NLC spinning strategy to prepare continuous locally aligned RGO fibers. These fibers showed smooth surfaces with a fine bark-like morphology and different shaped cross-sections with a tunable, locally aligned pore structure. Despite not being doped with nanofillers, they exhibited remarkably higher volume-specific capacitance than most of the neat and hybrid RGO fibers and CNT hybrid fibers prepared by conventional methods. And flexible solid-state supercapacitors assembled from these fibers possessed energy densities comparable to those of a commercial thin Li-film battery, while showed significantly higher power densities. We further demonstrated that a 3 V yarn supercapacitor can be integrated into a textile and was able to power a LED for several minutes after being charged. It is expected that these fibers will have great potential in a variety of applications, such as micro-batteries, sensors, actuators and wearable electronics. We also believe that the NLC spinning may be a general assembly method for the preparation of macroscopic fibers from various functional two-dimensional materials.

Acknowledgments

Appendix A.   Supporting information

Supplementary data associated with this article can be found in the online version at http://dx.doi.org/10.1016/j.nanoen.2015.05.004.

References

[1] K.S. Novoselov, V.I. Fal'Ko, L. Colombo, P.R. Gellert, M.G. Schwab, K. Kim, Nature 490 (2012) 192–200.

[2] M.D. Stoller, S.J. Park, Y.W. Zhu, J.H. An, R.S. Ruoff, Nano Lett. 8 (2008) 3498–3502.

[3] X.W. Yang, J.W. Zhu, L. Qiu, D. Li, Adv. Mater. 23 (2011) 2833–2838.

[4] L.M. Dai, Acc. Chem. Res. 46 (2013) 31–42.

[5] Y.X. Xu, Z.Y. Lin, X.Q. Huang, Y. Liu, Y. Huang, X.F. Duan, ACS Nano 7 (2013) 4042–4049.

[6] P. Chen, J.J. Yang, S.S. Li, Z. Wang, T.Y. Xiao, Y.H. Qian, S.H. Yu, Nano Energy 2 (2013) 249–256.

[7] Z. Yu, M. McInnis, J. Calderon, S. Seal, L. Zhai, J. Thomas, Nano Energy 11 (2015) 611–620.

[8] Y. Su, J. Du, D. Sun, C. Liu, H. Cheng, Nano Res. 6 (2013) 842–852.

[9] L. Liao, Y.C. Lin, M. Bao, R. Cheng, J. Bai, Y. Liu, Y. Qu, K.L. Wang, Y. Huang, X. Duan, Nature 467 (2010) 305–308.

[10] S. Stankovich, D.A. Dikin, G. Dommett, K.M. Kohlhaas, E.J. Zimney, E.A. Stach, R.D. Piner, S.T. Nguyen, R.S. Ruoff, Nature 442 (2006) 282–286.

[11] A. Bhattacharyya, S. Chen, M. Zhu, Express Polym. Lett. 8 (2014) 74–84.

[12] L.L. Li, S.H. Chen, W.J. Ma, Y.H. Cheng, Y.P. Tao, T.Z. Wu, W.P. Chen, Z. Zhou, M.F. Zhu, Express Polym. Lett. 8 (2014) 450–457.

[13] H.B. Li, L.D. Zou, L.K. Pan, Z. Sun, Environ. Sci. Technol. 44 (2010) 8692–8697.

[14] H.C. Bi, X. Xie, K.B. Yin, Y.L. Zhou, S. Wan, L.B. He, F. Xu, F. Banhart, L.T. Sun, R.S. Ruoff, Adv. Funct. Mater. 22 (2012) 4421–4425.

[15] L.P. Ma, Z.S. Wu, J. Li, E.D. Wu, W.C. Ren, H.M. Cheng, Int. J. Hydrog. Energ. 34 (2009) 2329–2332.

[16] G. Srinivas, Y.W. Zhu, R. Piner, N. Skipper, M. Ellerby, R. Ruoff, Carbon 48 (2010) 630-635.

[17] Z. Xu, C. Gao, Nat. Commun. 2 (2011).

[18] X. Li, T. Zhao, K. Wang, Y. Yang, J. Wei, F. Kang, D. Wu, H. Zhu, Langmuir 27 (2011) 12164-12171.

[19] Z. Xu, H. Sun, X. Zhao, C. Gao, Adv. Mater. 25 (2013) 188-193.

[20] Z. Dong, C. Jiang, H. Cheng, Y. Zhao, G. Shi, L. Jiang, L. Qu, Adv. Mater. 24 (2012) 1856-1861.

[21] M. Zhang, K.R. Atkinson, R.H. Baughman, Science 306 (2004) 1358-1361.

[22] S. Zhang, C. Ji, Z. Bian, R. Liu, X. Xia, D. Yun, L. Zhang, C. Huang, A. Cao, Nano Lett. 11 (2011) 3383-3387.

[23] J. Ren, L. Li, C. Chen, X. Chen, Z. Cai, L. Qiu, Y. Wang, X. Zhu, H. Peng, Adv. Mater. 25 (2013) 1155-1159.

[24] Q.H. Meng, K. Wang, W. Guo, J. Fang, Z.X. Wei, X.L. She, Small 10 (2014) 3187-3193.

[25] G. Sun, X. Wang, P. Chen, Mater. Today 18 (2015) 215-226.

[26] A.C. Schmidt, X. Wang, Y.T. Zhu, L.A. Sombers, ACS Nano 7 (2013) 7864-7873.

[27] Y.B. Li, Y.Y. Shang, X.D. He, Q.Y. Peng, S.Y. Du, E.Z. Shi, S.T. Wu, Z. Li, P.X. Li, A.Y. Cao, ACS Nano 7 (2013) 8128-8135.

[28] S.R. Shin, C.K. Lee, I. So, J. Jeon, T.M. Kang, C. Kee, S.I. Kim, G.M. Spinks, G.G. Wallace, S.J. Kim, Adv. Mater. 20 (2008) 466.

[29] J. Foroughi, G.M. Spinks, G.G. Wallace, J. Oh, M.E. Kozlov, S. Fang, T. Mirfakhrai, J.D.W. Madden, M.K. Shin, S.J. Kim, R. H. Baughman, Science 334 (2011) 494-497.

[30] Y. Meng, Y. Zhao, C. Hu, H. Cheng, Y. Hu, Z. Zhang, G. Shi, L. Qu, Adv. Mater. 25 (2013) 2326-2331.

[31] T.Q. Huang, B.N. Zheng, L. Kou, K. Gopalsamy, Z. Xu, C. Gao, Y.N. Meng, Z.X. Wei, RSC Adv. 3 (2013) 23957-23962.

[32] D.S. Yu, K. Goh, H. Wang, L. Wei, W.C. Jiang, Q. Zhang, L.M. Dai, Y. Chen, Nat. Nanotechnol. 9 (2014) 555-562.

[33] C. Xiang, C.C. Young, X. Wang, Z. Yan, C. Hwang, G. Cerioti, J. Lin, J. Kono, M. Pasquali, J.M. Tour, Adv. Mater. 25 (2013) 4592-4597.

[34] R. Jalili, S.H. Aboutalebi, D. Esrafilzadeh, R.L. Shepherd, J. Chen, S. Aminorroaya-Yamini, K. Konstantinov, A.I. Minett, J.M. Razal, G.G. Wallace, Adv. Funct. Mater. 23 (2013) 5345-5354.

[35] G. Huang, C. Hou, Y. Shao, B. Zhu, B. Jia, H. Wang, Q. Zhang, Y. Li, Nano Energy 12 (2015) 26-32.

[36] L. Kou, T.Q. Huang, B.N. Zheng, Y. Han, X.L. Zhao, K. Gopalsamy, H.Y. Sun, C. Gao, Nat. Commun. 5 (2014).

[37] G.Z. Sun, J.Q. Liu, X. Zhang, X.W. Wang, H. Li, Y. Yu, W. Huang, H. Zhang, P. Chen, Angew. Chem. Int. Ed. 53 (2014) 12576-12580.

[38] W.S. Hummers Jr., R.E. Offeman, J. Am. Chem. Soc. 80 (1958) 1339.

[39] J.J. Hermans, P.H. Hermans, D. Vermaas, A. Weidinger, Recl Trav. Chim. Pays-Bas 65 (1946) 427-447.

[40] R.S. Stein, J. Polym. Sci. 31 (1958) 327-334.

[41] P.T. Hang, G.W. Brindley, Clays Clay Miner. 18 (1970) 203-212.

[42] T. Szabo, E. Tombacz, E. Illes, I. Dekany, Carbon 44 (2006) 537-545.

[43] D. Li, M.B. Muller, S. Gilje, R.B. Kaner, G.G. Wallace, Nat. Nanotechnol. 3 (2008) 101-105.

[44] S. Pei, J. Zhao, J. Du, W. Ren, H.M. Cheng, Carbon 48 (2010) 4466-4474.

[45] A. Aygun, S. Yenisoy-Karakas, I. Duman, Micropor. Mesopor. Mat. 66 (2003) 189-195.

[46] M.J. McAllister, J.L. Li, D.H. Adamson, H.C. Schniepp, A.A. Abdala, J. Liu, M. Herrera-Alonso, D.L. Milius, R. Car, R.K. Prud'Homme, I.A. Aksay, Chem. Mater. 19 (2007) 4396-4404.

[47] S.H. Aboutalebi, R. Jalili, D. Esrafilzadeh, M. Salari, Z. Gholamvand, S.A. Yamini, K. Konstantinov, R.L. Shepherd, J. Chen, S.E. Moulton, P.C. Innis, A.I. Minett, J.M. Raza, G.G. Wallace, ACS Nano 8 (2014) 2456-2466.

[48] C. Xiang, N. Behabtu, Y. Liu, H.G. Chae, C.C. Young, B. Genorio, D.E. Tsentalovich, C. Zhang, D.V. Kosynkin, J.R. Lomeda, C. Hwang, S. Kumar, M. Pasquali, J.M. Tour, ACS Nano 7 (2013) 1628-1637.

[49] T.L. Viet, H. Kim, A. Ghosh, J. Kim, J. Chang, A.V. Quoc, T.P. Duy, J. Lee, S. Kim, Y.H. Lee, ACS Nano 7 (2013) 5940-5947.

[50] X. Lepro, R. Ovalle-Robles, M.D. Lima, A.L. Elias, M. Terrones, R.H. Baughman, Adv. Funct. Mater. 22 (2012) 1069-1075.

[51] Y.J. Oh, J.J. Yoo, Y.I. Kim, J.K. Yoon, H.N. Yoon, J.H. Kim, S.B. Park, Electrochim. Acta 116 (2014) 118-128.

[52] X.W. Yang, C. Cheng, Y.F. Wang, L. Qiu, D. Li, Science 341 (2013) 534-537.

[53] J.A. Lee, M.K. Shin, S.H. Kim, H.U. Cho, G.M. Spinks, G.G. Wallace, M.D. Lima, X. Lepro, M.E. Kozlov, R. H. Baughman, S.J. Kim, Nat. Commun. 4 (2013).

[54] D. Pech, M. Brunet, H. Durou, P.H. Huang, V. Mochalin, Y. Gogotsi, P.L. Taberna, P. Simon, Nat. Nanotechnol. 5 (2010) 651-654.

[55] M.F. El-Kady, V. Strong, S. Dubin, R.B. Kaner, Science 335 (2012) 1326-1330.

[56] X. Xiao, T. Li, P. Yang, Y. Gao, H. Jin, W. Ni, W. Zhan, X. Zhang, Y. Cao, J. Zhong, L. Gong, W. Yen, W. Mai, J. Chen, K. Huo, Y. Chueh, Z.L. Wang, J. Zhou, ACS Nano 6 (2012) 9200-9206.

[57] P.H. Yang, Y. Ding, Z.Y. Lin, Z.W. Chen, Y.Z. Li, P.F. Qiang, M. Ebrahimi, W.J. Mai, C.P. Wong, Z.L. Wang, Nano Lett. 14 (2014) 731-736.

[58] D.S. Yu, K.L. Goh, Q. Zhang, L. Wei, H. Wang, W.C. Jiang, Y. Chen, Adv. Mater. 26 (2014) 6790-6797.

Shaohua Chen received his Bachelor's degree in Polymer Science & Engineering from Donghua University in 2009. Currently he is a Ph.D. candidate under the supervision of Prof. Meifang Zhu at College of Materials Science & Engineering, Donghua University. His research focuses on the processing and structural control of nanocarbon-based fibers for flexible energy storage.

Wujun Ma received his Bachelor's degree from Wuhan Textile University in 2009 and Master degree in Textile Chemistry and Dyeing and Finishing Engineering from Soochow University in 2012. He is currently pursuing his Ph.D. under the supervision of Prof. MeiFang Zhu at College of Materials Science and Engineering, Donghua University. His research interests mainly focus on the synthesis and application of graphene-based materials for flexible supercapacitors.
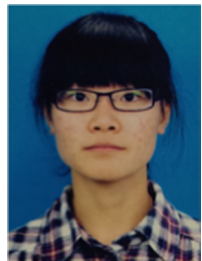
Yanhua Cheng received her Bachelor's degree from the College of Materials Science and Engineering at Donghua University in 2008. She is currently pursuing her Ph.D. under the supervision of Prof. Meifang Zhu at Donghua University. Her research interests mainly focus on polymer-assisted synthesis of metal oxide-carbon hybrid materials for lithium-ion battery anodes.

Zhe Weng received his Bachelor's degree in Materials Science and Engineering and Master degree in Materials Science from Huazhong University of Science & Technology, Wuhan, China in 2006 and 2008, and Ph.D. in Materials Science from Institute of Metal Research, Chinese Academy of Sciences in 2013 supervised by Prof. Hui-Ming Cheng. He is currently a postdoctoral fellow working with Prof. Hailiang Wang at Department of Chemistry and Energy Sciences Institute, Yale University, USA. His research mainly focuses on synthesis and application explorations of carbon-based nanomaterials for energy storage and conversion systems in supercapacitors, batteries and electrocatalysis.

Bin Sun received his Ph.D. degree in Materials Science from College of Materials Science and Engineering, Donghua University (DHU) in 2004. He has been an assistant and associate professor of materials science at DHU since 2004. From 2007 to 2009, he worked with Prof. Stephen Z.D. Cheng at the University of Akron as a visiting researcher. His current research interests include the preparation, properties and applications of functional nanohybrids, especially in the fiber modification field.

Lu Wang received her Bachelor's degree in Composite Materials Engineering from Donghua University in 2014. She is currently pursuing her Master degree in Materials Engineering at Donghua University. Her research interest mainly focuses on synthesis and application of graphene-based materials for capacitive deionization.

Wenping Chen received her Ph.D. degree in Materials Science from Donghua University (DHU), Shanghai, China, then joined its faculty in 2006. She is an associate professor of College of Materials Science and Engineering at DHU since 2013. Her research interests focus mainly on the structure formation in polymer fiber processing, the structure-property relationship of polymer fibers and functional fibers.

Feng Li is a professor of the Institute of Metal Research, Chinese Academy of Sciences (IMR, CAS). He received his Ph.D. in materials science at IMR, CAS in 2001 supervised by Prof. Hui-Ming Cheng. He focuses on the design, synthesis and electrochemical energy storage applications (including lithium ion battery, supercapacitor and lithium sulfur battery) of carbon nano-materials. He has explored and developed carbon-based flexible electrodes and electrochemical devices and achieved the commercialization of carbon-coated electrode materials.

Meifang Zhu received her Ph.D. from Donghua University (DHU) in 1999 after jointly studying at DHU and Dresden University of Technology (TU, Dresden), Germany. She has worked at DHU since 1989 and partially worked at TU, Dresden from 1999 to 2009. Currently she is a full professor and Dean of College of Materials Science & Engineering at DHU as well as Director of State Key Laboratory for Modification of Chemical Fibers and Polymer Materials. Her research focuses on hybrid fibers/resins/hydrogels for applications in personal healthcare, occupational protection, biomedicine, environmental protection and wearable energy storage.

Hui-Ming Cheng received his Ph.D. in Materials Science from the Institute of Metal Research, Chinese Academy of Sciences (IMR, CAS). He worked at AIST and Nagasaki University in Japan, and MIT in USA, in 1990s. Currently he is Professor and Director of the Advanced Carbons Research Division at Shenyang National Laboratory for Materials Science, IMR, CAS. His research interests focus mainly on carbon nanotubes, graphene, high-performance bulk carbons, energy storage materials, and photocatalytic materials for hydrogen production and CO_2 conversion.